RSC Advances

PAPER

View Article Online
View Journal | View Issue

Cite this: *RSC Adv.*, 2025, **15**, 37999

Optoelectronic and thermoelectric response of lead-free halide double perovskites Rb_2BiAuX_6 (X = Cl, Br, I) for energy storage applications

Farooq Ali,[a] Mubashir Hussain,[b] Hamid Ullah, *[a] Jian-Tao Wang [cde] and Muneerah Alomar[f]

Double perovskite materials garner a lot of attention because of their extraordinarily high conversion efficiency in solar cells. Here, we report a detailed first-principles study on the structural, mechanical, optoelectronic, and thermal characteristics of Rb_2BiAuX_6 (X = Cl, Br, and I) lead-free halide double perovskites. $Rb_2BiAuCl_6$ exhibits more favorable nature than the other two materials owing to its lowest formation energy. Rb_2BiAuX_6 (X = Cl, Br, and I) possess mechanical stability, supported by their high elastic constants. Interestingly, these double perovskites reveal a semiconductor nature with a band gap of 1.8 eV, 1.12 eV, and 0.61 eV for $Rb_2BiAuCl_6$, $Rb_2BiAuBr_6$, and Rb_2BiAuI_6, respectively. The high absorption peaks in their optical spectra confirm their suitability for solar cells applications. $Rb_2BiAuCl_6$ demonstrates a higher *ZT* value of 0.78 at 300 K compared to the other two materials. Furthermore, thermodynamics analysis confirm their suitable behavior under varying pressure and temperature. These results suggest the potential of these double perovskites for promising applications in solar cells and thermal devices.

Received 24th June 2025
Accepted 18th September 2025

DOI: 10.1039/d5ra04508h

rsc.li/rsc-advances

1. Introduction

The need for clean and renewable energy sources, as well as the growing demand and limited availability of energy, have spurred researchers to investigate new material classes.[1,2] Because of the limitations of current energy sources and their consequences on our economy and environment, there is an increasing desire to look at renewable energy solutions as a way to achieve sustainable development.[3] The scientific community has recently given solar energy a great deal of attention because of the depletion of conventional energy sources and the rising global energy demand. With its clean and renewable nature, solar energy essentially eliminates the need for more traditional energy sources like coal, natural gas, and fossil fuels.[4] Instead, it provides a sustainable alternative.

Double perovskites (DP) have garnered a lot of attention from scientists lately because of their extraordinarily high conversion efficiency.[1,2] In 2009, double perovskite solar cells with a 3.8% conversion efficiency were introduced to the optoelectronics market.[5] Efficiency has increased dramatically since then, reaching levels above 25% so far. A novel class of perovskite variations has surfaced recently that offers a competitive advantage over traditional perovskite solar cells. These substitute perovskite forms, also referred to as double perovskites, are distinguished by their all-inorganic makeup, which excludes the usage of lead.[1] Generally, perovskites are represented by the general formulas A_2BX_6 or $A_2BB'X_6$, where A denotes an inorganic cation, B is a tetravalent cation, BB′ is a combination of monovalent and trivalent cations, and X is a halide. The stability of solar cells composed of double perovskites is enhanced by the greater flexibility offered by the diverse inorganic options accessible at the A site.

The B site in double perovskites can be replaced by elements other than lead, such as Bi, Sn, Ge, Cu, and alkaline metal elements (such as Ca, Ba, and Sr).[1,6–9] Two major prerequisites must be met in order to increase the effectiveness of energy cells and photovoltaic systems based on double perovskites halides. First, a narrow band gap between 0.8 and 2.2 eV is needed,[10] as better light conversion efficiencies[11] are only displayed by good

[a]*Department of Physics, Riphah International University Islamabad, Lahore Campus, Pakistan. E-mail: hamid.uou@gmail.com*

[b]*Department of Physics, University of Lahore, Lahore, Pakistan*

[c]*Beijing National Laboratory for Condensed Matter Physics, Institute of Physics, Chinese Academy of Sciences, Beijing, 100190, China*

[d]*School of Physical Sciences, University of Chinese Academy of Sciences, Beijing, 100049, China*

[e]*Songshan Lake Materials Laboratory, Guangdong, 523808, China*

[f]*Department of Physics, College of Science, Princess Nourah Bint Abdulrahman University, P. O. Box 84428, Riyadh, 11671, Saudi Arabia*

He obtained his PhD from the University of Ulsan, Republic of Korea, in 2020. Now, he is a Postdoctoral fellow at the Chinese Academy of Science, China. Dr Hamid's research area focuses on computational physics, chemistry, and materials.

light absorbers with band gaps between 1.3 and 1.7 eV. Second, a direct band gap is essential for raising the light conversion efficiency of the photovoltaic absorbers.[12]

Among the huge number of DPs, the most promising double perovskite halides for commercial applications are those like Rb_2BiAuX_6 (X = Cl, Br, I), as it possesses an indirect band gap and a strong absorption edge.[13] Because the electronic energy states occur relatively far from the band boundaries, as is typically seen in perovskites of the ABX_3 type, the Rb cation at the A-site serves as a spacer. Since an increase in the ionic radius decreases the energy band gap, halide ions may produce band gap tuning.[14] Notably, the nature of the band gaps, both direct and indirect, is independent of the cations and anions present in the A-site. For instance, Kamal *et al.*[15] reported on a band gap in the range from 0.17 eV to 0.61 eV for Rb_2BiAuX_6 (X = Cl and Br). Moreover, the band gap varies with different cations. For K_2AuBiX_6 (X = F, Cl, Br, and I), they reported band gaps of 1.16 eV, 1.14 eV, and 1.12 eV, respectively.[16] A lot of literature is available on the band gap tuning with the alteration of cations.[17–20] One can observe the discrepancies in the band gap in these materials, which motivated us to conduct a systematic study of the perovskites.

In this work, we have systematically investigated the structural, mechanical, optoelectronic, thermal, and thermodynamic characteristics of Rb_2BiAuX_6 (X = Cl, Br, and I) by first-principles calculations. Our findings show that these double perovskites may be promising for applications in solar cells and thermal devices.

2. Computational methods

The study makes use of density functional theory (DFT) as it is implemented in the Wien2K code.[21] Density functional theory's Kohn–Sham equations are solved using the FP-LAPW method.[22] The exchange and correlation functionals of Perdew–Burke–Ernzerhof (PBE-sol) GGA have been considered for relaxing the structural parameters.[23] The muffin-tin radius values of Rb^+ = 2.50, Bi^{3+} = 2.50, Au^+ = 2.50, Cl^- = 2.13, Br^- = 2.37, and Cl^- = 2.50 are chosen. In this investigation, we obtain a band gap that is comparable to the experimental one. The Trans–Blaha modified Becke–Johnson (TB-mBJ) approximation[24,25] potential-based self-consistent field (SCF) converges the entire energy of the systems with proper energy and charge convergence criteria of 0.0001 and 0.00001, respectively. Additionally, we performed the spin–orbit coupling along with the mBJ (mBJ + SOC)[24,25] to see the effect of SOC on the electronic properties. We have considered the standard LO and RLO in SOC calculations, which automatically place the linearization energy at the current eigenenergy for the d-orbital. We use the finite displacement method with a 4 × 6 × 3 supercell to obtain the phonon spectra and analysed it using the Phonopy code[26] with the Vienna *ab initio* Simulation Packages (VASP)[27,28] as a calculator. Additionally, for the *ab initio* molecular dynamics (MD) simulation, we used the Nose–Hoover heat bath scheme[29] with a step rate of 1 fs. We computed the electronics, optical, thermoelectric, and transport using the modified Becke–Johnson (mBJ) potential.[30] We have used *k*-points with a 12 × 12 × 12 mesh to sample the Brillouin zone. The thermoelectric properties are estimated by solving the Boltzmann equation with a rigid band approximation using the BoltzTrap package.[31] Additionally, we have employed the Gibbs2[32] package to investigate the thermodynamics properties of Rb_2BiAuX_6 (X = Cl, Br, I).

3. Results and discussions

3.1. Structure and stability of Rb_2BiAuX_6 (X = Cl, Br, I)

The face-centered cubic structure of Rb_2BiAuX_6 (X = Cl, Br, I) has the $Fm\bar{3}m$ space group (#225). As shown in Fig. 1, the unit cell contains eight Rb atoms occupying the 8c (0.25, 0.25, 0.25), four Bi atoms occupying the 4a (0.0, 0.0, 0.0), four Au atoms occupying the 4b (0.5, 0.5, 0.5), and 24 X atoms occupying the 24e (0.0, 0.25, 0.5) Wyckoff positions. It is worth noting that the double perovskite compounds adopt the $A_2BB'O_6$-type structure with O replaced by halogens: Cl, Br, I).[1,9,33] This structure is highly tunable and relevant for optoelectronic applications (*e.g.*, solar cells, LEDs).[2,34] The selection of Rb_2AuBiX_6 (X = Cl, Br, I) for our study is typically driven by a combination of theoretical interest, material stability, and targeted electronic properties. The Rb^+ cation stabilizes the perovskite framework, while Au^{3+} and Bi^{3+} occupy the B/B′ sites, creating an ordered arrangement. Au^{3+} and Bi^{3+} are isovalent, ensuring charge neutrality without defects. This simplifies the DFT modeling. Bismuth is a low-toxicity "green element" compared to lead (Pb) or thallium (Tl), aligning with research into eco-friendly materials.[34]

To get the cubic lattice constants at the ground state, the optimal volumes for each of the three double perovskites are computed prior to calculating the physical properties. The curves of the volume optimization exhibit the equilibrium states of Rb_2BiAuI_6 with a volume of 424 Å^3 per f.u., followed by $Rb_2BiAuBr_6$ with a volume of 350 Å^3 per f.u., and $Rb_2BiAuCl_6$ with a volume of 303 Å^3 per f.u. at ground state, as shown in Fig. 1. Additionally, we have estimated the formation energy of Rb_2BiAuX_6 (X = Cl, Br, I) to check their relative stability. We have used the relation, $E_f = [E_{Rb_2BiAuX_6} - n\{2E_{Rb} + E_{Bi} + E_{Au} + 6E_X\}]/N$, where $E_{Rb_2BiAuX_6}$, E_{Rb}, E_{Bi}, E_{Au}, and E_X represent the total energy of Rb_2BiAuX_6 (X = Cl, Br, I) per unit cell, and the energy of the isolated Rb Bi, Au, and the X atoms in their elemental phase, correspondingly, N is the total number of atoms in the unit cell, and $n = 4$ is the number of formula units per unit cell. We have estimated the E_f values to be −1.58 eV per f.u, −1.41 eV per f.u., and −1.08 eV per f.u. for $Rb_2BiAuCl_6$, $Rb_2BiAuBr_6$, and Rb_2BiAuI_6, respectively. Our findings are compared with the current state of research on $K_2RbTlBr_6$ (−1.62 eV),[35] $Cs_2InAuCl_6$ (−1.38 eV)[9] and $Cs_2InAuBr_6$ (−1.34 eV).[9] Thus, our calculated E_f values exhibit the stable nature of Rb_2BiAuX_6 (X = Cl, Br, I) and can be easily incorporated in experiments. In comparison to $Rb_2BiAuBr_6$ and Rb_2BiAuI_6, $Rb_2BiAuCl_6$ possesses the lowest formation energy. Thus, $Rb_2BiAuCl_6$ could be easily incorporated in experiments.

To further assess the stability of the Rb_2AuBiX_6 (X = Cl, Br, I) structure, we carried out the phonon dispersion calculations. The calculated phonon band spectrum along the high symmetry directions (W–L–Γ–X–W–K) of the Brillouin zone confirms the

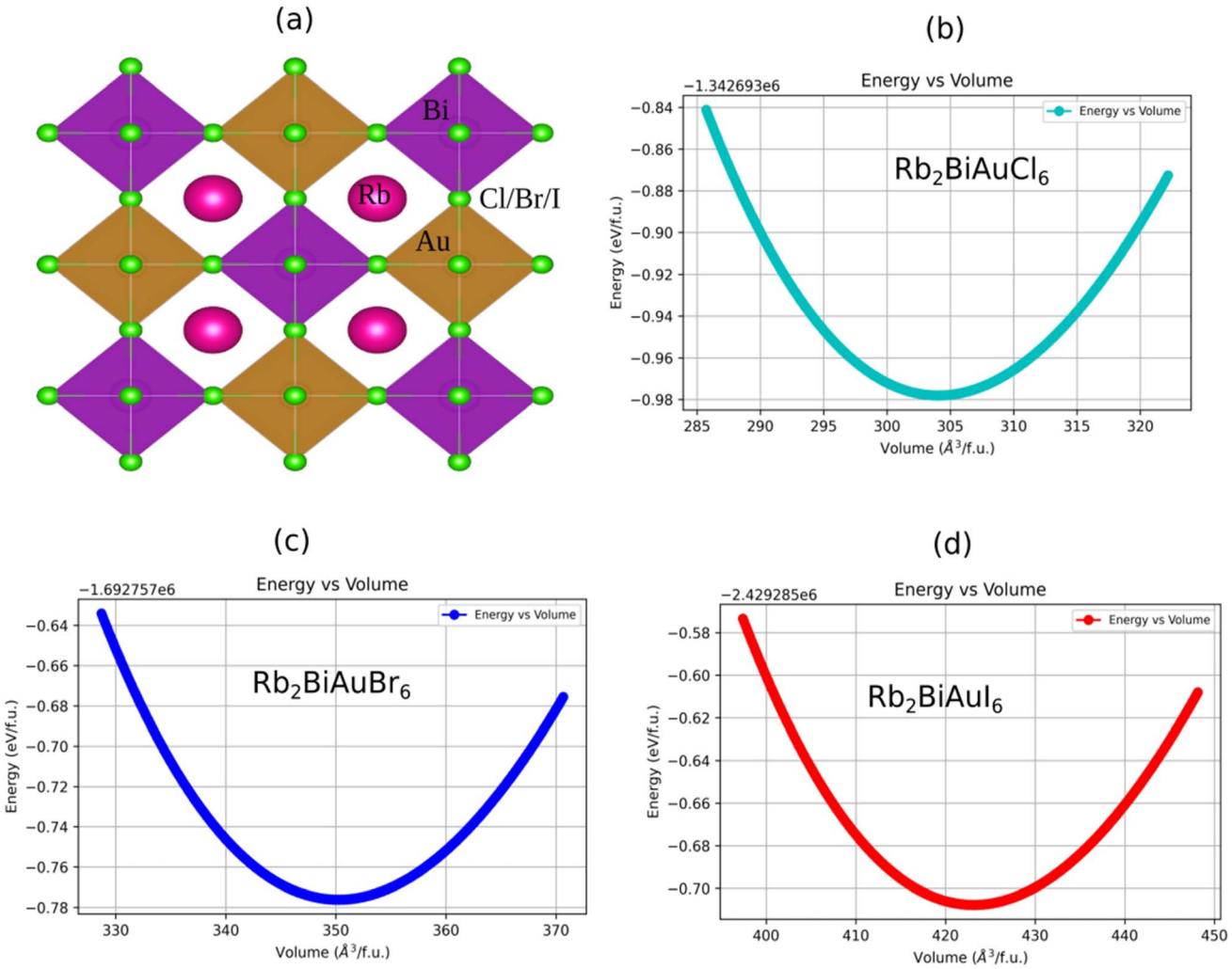

Fig. 1 (a) Optimized crystal structure ($Fm\bar{3}m$) with the (b–d) energy–volume curves of Rb_2BiAuX_6 (X = Cl, Br, and I).

absence of an imaginary frequency at the Γ-point, indicating the dynamic stability of the corresponding compounds, as shown in Fig. 2(a–c). Our calculated phonons are analogous to those of Cs_2InSbX_6 (X = Cl, Br, and I)[36] and Cs_2InBiX_6 (X = Cl, Br, and I).[37]

Additionally, to verify the thermodynamic stability of Rb_2AuBiX_6 (X = Cl, Br, I), we have performed *ab initio* finite temperature molecular dynamics (MD) simulation at 500 K for 8000 steps with a time step of 1 fs using the Nose–Hoover heat bath scheme.[29,38] In order to reduce the periodic constraints, we have used a supercell of 5 × 5 × 2. We can see the fluctuation of the total energy of compounds as a function of simulation steps. The average values of the total energy remain nearly constant during simulation, as shown in Fig. 2. It is observed that the atomic structures are well-sustained during the simulation process.

3.2. Mechanical properties

The mechanical (elastic) characteristics of a material and its stability are frequently evaluated using the elastic constants (C_{ij}). This property describes how a material undergoes a change under stress before returning to its initial state when the strain is removed. It is crucial to disclose details on the structural stability, anisotropic properties, and the binding properties between neighboring atomic planes. Three independent elastic constants, C_{11}, C_{12} and C_{44}, define a compound in cubic form. Every calculated elastic constant satisfies the given Born stability criteria ($C_{44} > 0$, $C_{11}–C_{12} > 0$, and $C_{11} + 2C_{12} > 0$),[39] suggesting that every compound under investigation is mechanically stable.

In order to determine the basic mechanical characteristics of Rb_2BiAuX_6 (X = Cl, Br, I), the computed C_{ij} parameters are listed in Table 1. These properties include the shear modulus (G), bulk modulus (B), Young's modulus (Y), Pugh's ratio ($k = B/G$), Pugh's modulus (G/B), anisotropic ratio (A), and Poisson's ratio (ν). The Voigt–Reuss method is taken into account to calculate the bulk modulus (B) and shear modulus (G). According to Hill theory,[40] the bulk modulus and shear modulus are arithmetic means of Voigt–Reuss expressions. Additionally, Young's modulus (Y) and Poisson's ratio (ν) are calculated by the expression described elsewhere.[40] The B and G describe the

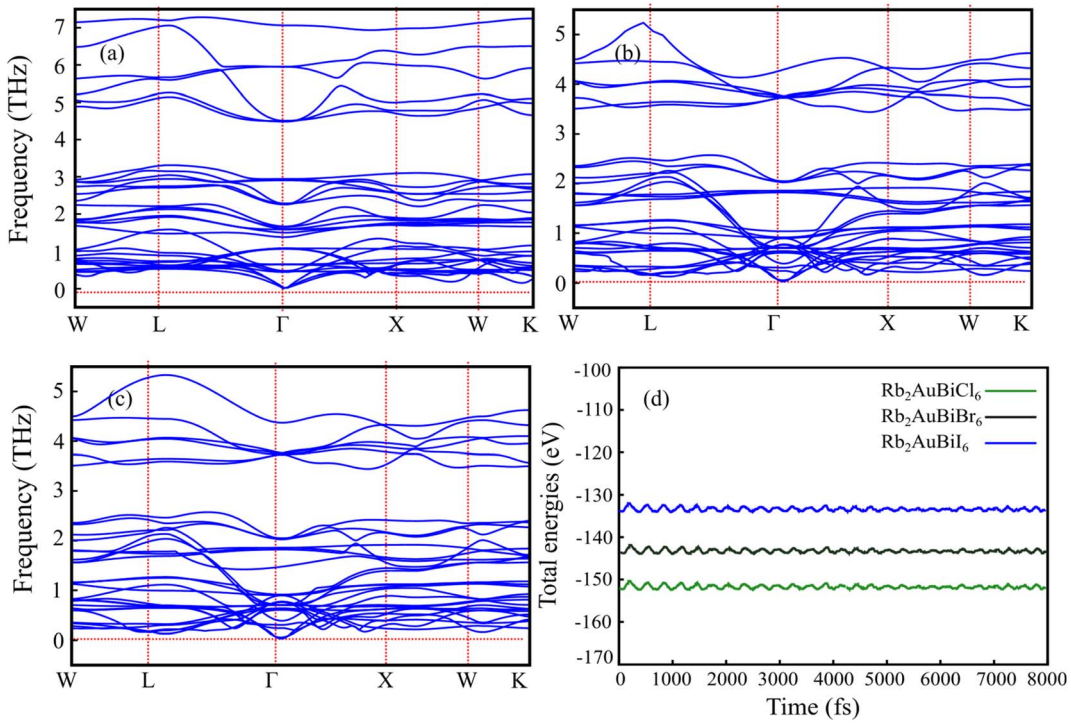

Fig. 2 The calculated phonon spectra for (a) $Rb_2AuBiCl_6$, (b) $Rb_2AuBiBr_6$, (c) Rb_2AuBiI_6, and (d) the AIMD simulation for Rb_2AuBiX_6 (X = Cl, Br, and I).

Table 1 The estimated values of the elastic parameters and calculated Debye temperature (θ_D), longitudinal (v_l) and transverse velocities (v_t), average sound velocity (v_m), and calculated deformation potential (E_{1c} and E_{1v} for the electron and hole, respectively), elastic constant (c_{ii}), and carrier mobility (μ_e and μ_e for the electron and hole, respectively) of Rb_2BiAuX_6 (X = Cl, Br and I)

Parameters	$Rb_2BiAuCl_6$	$Rb_2BiAuBr_6$	Rb_2BiAuI_6
a_0 (Å)	10.660	11.185	11.926
C_{11} (GPa)	37.22	39.90	34.80
C_{12} (Gpa)	27.60	22.09	16.84
C_{44} (Gpa)	6.50	6.07	5.98
B (Gpa)	30.81	28.02	22.82
G (Gpa)	5.83	7.20	7.18
Y (Gpa)	16.44	19.90	19.49
B/G	5.29	3.89	3.18
G/B	0.41	0.38	0.36
A	1.35	0.68	0.66
ν	0.41	0.38	0.36
θ_D (K)	126.0	122.4	112.2
v_t (m s^{-1})	1184.2	1194.7	1176.9
v_l (m s^{-1})	3060.8	2748.4	2517.4
v_m (m s^{-1})	1342.8	1349.4	1325.0
E_{1c} (eV)	−4.60	−7.60	−7.80
E_{1v} (eV)	−6.41	−6.76	−7.77
μ_e (10^3 cm^2 V^{-1} s^{-1})	22.17	16.37	26.00
μ_h (10^3 cm^2 V^{-1} s^{-1})	6.24	15.51	9.60

fracture resistance and deformation of plastic, respectively. For Rb_2BiAuX_6 (X = Cl, Br, I), our computed values of B and G are significantly higher than those of Rb_2AgPX_6 (X = Cl, Br, I),[1] as described in the literature. It illustrates that the Rb_2BiAuX_6 (X = Cl, Br, and I) series of complexes are more resistant to plastic deformation and fracture than the previously described materials. The material stiffness is described by the term Y. So, according to the Young's modulus value, Rb_2BiAuI_6 should be much stiffer than $Rb_2BiAuCl_6$ and $Rb_2BiAuBr_6$. Materials with a ν value of 0.25 suggest the presence of ionic character, whereas those with a ν value of 0.1 mostly display covalent bonding.[41] The Rb_2BiAuX_6 (X = Cl, Br, I) series reveal the ionic character with ν values of 0.41, 0.38, 0.36, respectively. Our ν values are comparable with the available literature on Rb_2AgPX_6 (X = Cl, Br, I) ranging from 0.29–0.52,[1] and 0.4 for $Rb_2InGaCl_6$.[33] The ratio of the bulk modulus to the shear modulus, or B/G, is calculated to produce Pugh's ratio, which is used to evaluate the material's mechanical behavior. Materials beyond this threshold are considered ductile, while those below are considered brittle.[42] Another important parameter to justify the ductility or brittleness of the materials is B/G, which has a critical value of 1.75. So, $Rb_2BiAuCl_6$ has greater ductility than $Rb_2BiAuBr_6$ and Rb_2BiAuI_6. Additionally, our results are consistent with data on Poisson's and Pugh's ratios of compounds such as Mg_2BeTMH_8 (ref. 43) and $X_4Mg_4H_{12}$ (ref. 44) that have been previously reported. The rate of elastic anisotropy in cubic structures is defined by the factor A. $A = 1$ denotes the compound's entire isotropy. On the other hand, the material is considered anisotropic if it is more than or less than 1.[45] For Rb_2BiAuX_6 (X = Cl, Br, I), the estimated values of A indicate that anisotropic behavior is revealed in the crystal.

I stability of the Rb_2BiAuX_6 (X= Cl, Br, I) series is also confirmed by the Debye temperature (θ_D). From the tensor

matrix of Charpin, the value of θ_D could be computed in terms of the average sound velocity, as given in the relation below;[46,47]

$$\theta_D = \left(\frac{h}{k_B}\right)\left(\frac{3n}{4\pi}\frac{N_A\rho}{M}\right)^{\frac{1}{3}} v_m$$

where M is the molar mass, N_A is Avogadro's number, ρ is density, and the average sound velocity is presented by v_m.

From the transverse parts of the Navior equations v_t and the longitudinal v_l, the average sound velocity can be determined by the following relation:

$$v_m = \left(\frac{1}{3}\left(\frac{2}{v_t{}^3} + \frac{1}{v_l{}^3}\right)\right)^{-\frac{1}{3}}$$

Here, the longitudinal (v_l) and transverse velocities (v_t) can separately be expressed as follows:

$$v_t = \left(\frac{G}{\rho}\right)^{\frac{1}{2}}$$

$$v_l = \left(\frac{(3B + 4G)}{\rho}\right)^{\frac{1}{2}}$$

The computed value are expressed in Table 1. The calculated s θ_D and sound velocities provide valuable information on the lattice dynamics and thermal transport properties of the Rb_2BiAuX_6 (X = Cl, Br, I) double perovskites. The θ_D is directly related to the highest vibrational frequency of the lattice and reflects the stiffness of the crystal. A higher θ_D indicates stronger interatomic bonding and lower lattice anharmonicity, which are favorable for enhanced thermal conductivity. Among the studied compounds, $Rb_2BiAuCl_6$ shows the highest Debye temperature (126 K), consistent with its wider band gap and relatively stronger bonding strength compared to the Br and I analogs. Conversely, Rb_2BiAuI_6 exhibits the lowest Debye temperature (112 K), suggesting weaker bonding and softer lattice vibrations, which can enhance the phonon scattering and lower the lattice thermal conductivity.

The v_l and v_t sound velocities describe the propagation of acoustic phonons in different vibrational modes, while v_m provides an effective measure for thermal transport modeling, particularly in the Debye approximation. The observed trend of slightly decreasing velocities from Cl to I is consistent with increasing atomic mass and lattice softness along the halide series. These results are physically significant as they highlight the interplay between crystal bonding, phonon transport, and thermal conductivity, thereby providing insights into the suitability of these double perovskites for thermoelectric and thermal management applications.

3.3. Electronic properties

To better understand the electronic properties of Rb_2BiAuX_6 (X = Cl, Br, I), we explore the electronic band structure and density of states (states/eV). From Fig. 2, one can see that the valence-band maximum (VBM) lies at the X symmetry point and the conduction-band minimum (CBM) lies at the L point, confirming the indirect band gap nature of Rb_2BiAuX_6 (Cl, Br, I). The electronic band gaps are computed to be 1.8 eV, 1.12 eV, and 0.61 eV for $Rb_2BiAuCl_6$, $Rb_2BiAuBr_6$, and Rb_2BiAuI_6, respectively, as shown in Fig. 3(a–c). The calculated band gaps of Rb_2BiAuX_6 are comparable with the previously reported double perovskite material Rb_2AgPX_6 (X = Cl, Br, I) in the range of 0.61 eV–1.60 eV,[1] and $Cs_2InAuCl_6$ (0.7 eV).[9] The computed results also fall within or close to the optimal range for single-junction photovoltaic absorbers (Shockley–Queisser limit: ~1.34 eV).[48] Although Rb_2BiAuX_6 (X = Cl, Br, I) exhibits an indirect band gap, this can be advantageous for photovoltaic and thermoelectric applications because it leads to reduced radiative recombination and longer carrier lifetimes, improving the charge extraction efficiency.[49–51] Furthermore, the systematic tunability of the band gap from 1.30 eV to 0.48 eV by halide substitution (Cl → Br → I) demonstrates chemical flexibility,

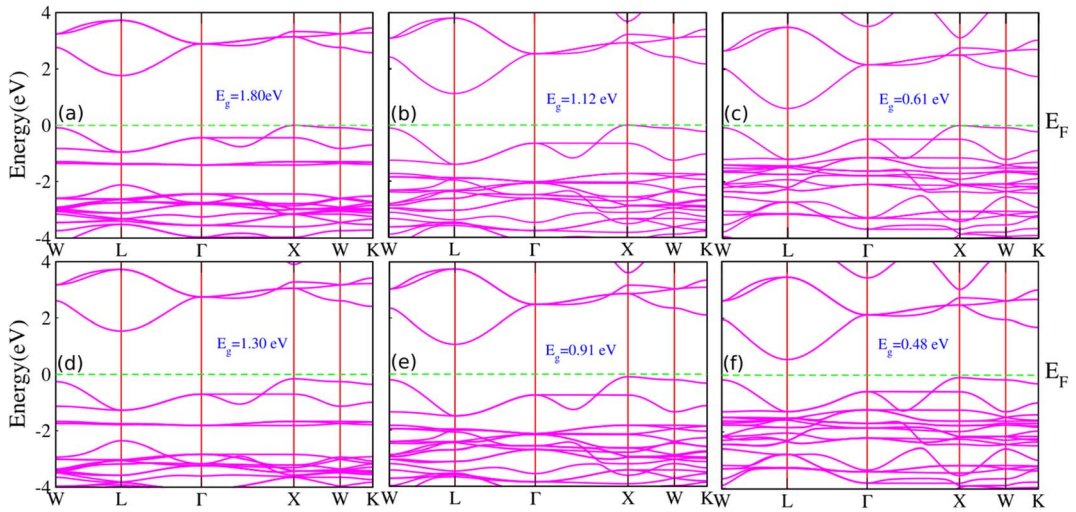

Fig. 3 The calculated electronic band structures of (a–d) $Rb_2BiAuCl_6$, (b–e) $Rb_2BiAuBr_6$, and (c–f) Rb_2BiAuI_6. Here, the top panel (a–c) represents the band structure without SOC, and the bottom panel (d–f) shows the band structure with SOC.

enabling potential broad-spectrum light harvesting. These combined factors of indirect band gap, chemical tunability, and favorable optical absorption distinguish the Rb_2BiAuX_6 series from most reported lead-free perovskites, highlighting their promise for high-efficiency photovoltaic applications. Moreover, we have estimated the effective mass following ref. 52. The calculated values of the electronic effective mass (m_e) are $0.11m_0$, $0.08m_0$ and $0.06m_0$ for $Rb_2BiAuCl_6$, $Rb_2BiAuBr_6$ and Rb_2BiAuI_6, respectively. However, for the hole (m_h), the values of the effective mass are found to be $0.14m_0$, $0.09m_0$ and $0.09m_0$ for $Rb_2BiAuCl_6$, $Rb_2BiAuBr_6$ and Rb_2BiAuI_6, respectively. Our calculated values are less than the m_e (0.19–0.58m_0) and m_h (0.25–0.64m_0) for $X_2ScCuCl_6$.[52] In order to calculate the transfer efficiency of the charge carriers in Rb_2BiAuX_6 (X= Cl, Br, I), we systematically studied the carrier mobility of Rb_2BiAuX_6 (X= Cl, Br, I). An easy approach based on the deformation potential (DP) theory is used to analyze the transport behaviour by using the following relation;[53]

$$\mu = \frac{(8\pi)^{\frac{1}{2}}\hbar^4 e c_{\{ii\}}}{3(m^*)^{\frac{5}{2}}(k_B T)^{\frac{3}{2}}E_1^{\,2}}$$

where the deformation potential is E_1, the temperature is T, the element charge is e, the elastic constant is $c_{\{ii\}}$, the effective mass of charge is m*, the Boltzmann constant is k_B, and the reduced Planck constant is $\hbar$. The energy shift of the band energy position (ΔE) with regard to a small lattice dilation (Δl) along a lattice (l_o) direction is known as the deformation potential $E_1 = \frac{\Delta E}{\Delta l / l_o}$. It should be noted that accurate band topologies are crucial for carrier mobility estimates. The energy shift of the band-edge states is calculated by aligning the core levels and using the mBJ potential, while taking the SOC effect into account. The computed carrier mobility and the deformation potential are listed in Table 1.

The computed electron mobilities are 22.17 $\times$ 10^3 cm^2 V^{-1} s^{-1}, 16.37 $\times$ 10^3 cm^2 V^{-1} s^{-1}, and 25.99 $\times$ 10^3 cm^2 V^{-1} s^{-1} for $Rb_2BiAuCl_6$, $Rb_2BiAuBr_6$, and Rb_2BiAuI_6, respectively, significantly higher than the experimentally measured value. Additionally, our findings are in line with another theoretical work, which predicted the higher carrier mobilities to be (7–30) $\times 10^3$ cm^2 V^{-1} s^{-1} (ref. 53) for electrons and 5.50 $\times$ 10^3 cm^2 V^{-1} s^{-1},[53] 14.47 $\times$ 10^3 cm^2 V^{-1} s^{-1} (ref. 54) for holes from a simplified Kane model. The high mobilities for the electron and hole are both due to the small effective masses (see Table 1), which can be inferred from the calculated band structure. Our calculated values are in good agreement with the available literature.[53,54]

Additionally, we performed spin–orbit coupling calculations for Rb_2AuBiX_6 (X = Cl, Br, I), which dramatically alters the electronic band structure primarily by reducing the band gap, as elucidated in Fig. 3(d and f). In the case of Rb_2BiAuX_6 (X = Cl, Br, I), the reduction of the band gap upon inclusion of spin–orbit coupling (SOC) originates from the strong relativistic effects associated with the heavy Bi and Au atoms. Without SOC, the valence band maximum (VBM) is primarily composed of halogen p states hybridized with 6s/6p-Bi and 5d-Au orbitals, while the conduction band minimum (CBM) has dominant 6p-Bi or 6p-Au contributions. When SOC is considered, the p and d orbitals of these heavy atoms undergo a substantial *j*-splitting, which raises the energy of certain VBM states (mainly $p_{3/2}$) and lowers the CBM states (mainly $p_{1/2}$). This combined effect narrows the band gap. Furthermore, the magnitude of the

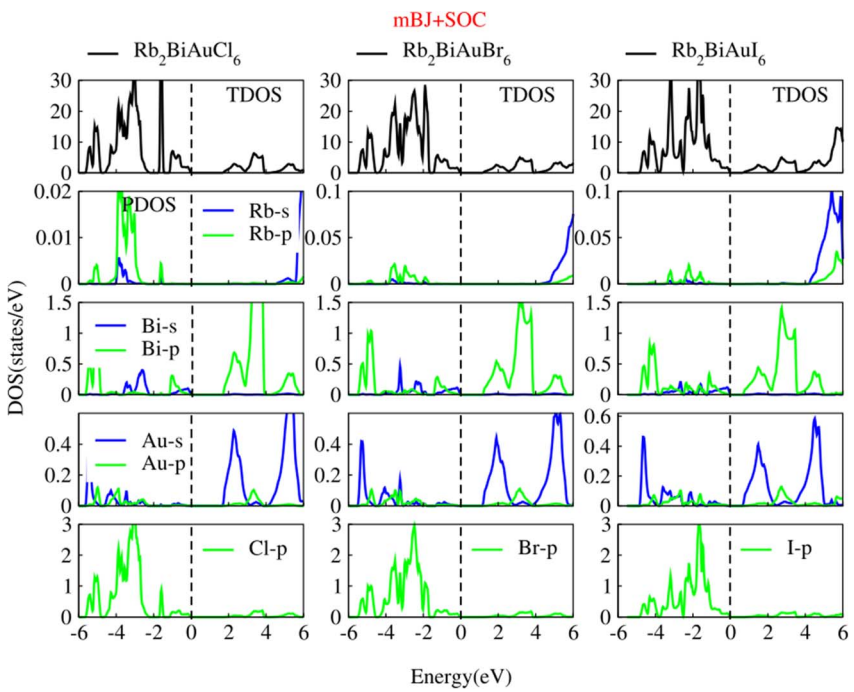

Fig. 4 The total and projected DOS of $Rb_2BiAuCl_6$ (left panel), $Rb_2BiAuBr_6$ (middle panel), and Rb_2BiAuI_6 (right panel) employing mBJ + SOC. The vertical black dotted line represent the Fermi-level.

reduction increases from Cl to Br to I due to the increasing SOC strength in the halogen p orbitals, with I exhibiting the largest effect. Similar SOC-driven gap reductions have been widely reported for other heavy-metal halide perovskites.[55,56]

Fig. 4 shows the total/projected density of states (TDOS/PDOS) of Rb_2BiAuX_6, which we determined based on the band structure, as well as the contribution of electrons from the various states to further explore the electronic properties. The s-/p-states of the Bi and Cl/Br/I atoms are dominant in the lower VB, and a negligibly small contribution can be seen from the s-/p-states of the Au atom to the TDOS. The major contribution near the VBM comes from the p-state electrons of the Bi and Cl atoms. The p-states of the Bi and Au atoms contribute to the lower CB, and there is a negligible contribution to the DOS from the s-states of Bi and Cl/Br/I. Moreover, the Au s-states contributed highly to the TDOS near the Fermi level. From Fig. 4, one can see that Rb_2BiAuX_6 (Cl, Br, I) possesses a semiconductor nature.

3.4. Optical properties

The semiconductor material's optical properties include reflectivity, conductivity, energy loss factors, absorption, and dielectric function.[57] Electrons can undergo intraband and interband transitions, which are two distinct types of transitions. The first one describes the metallic behavior of the materials, whereas the second one has to do with the semiconducting character.[58–60] Understanding the interaction between photons and electrons in a material requires an understanding of its optical nature, which is explained by its dielectric function.[61,62] The dielectric function's real (ε_1) and imaginary (ε_2) parameters are expressed as follows: for pristine, $\varepsilon(\omega) = \varepsilon_1(\omega) + i\varepsilon_2(\omega)$.[63] When a photon interacts with a material, the polarization and dispersion phenomena are described by the dielectric function's $\varepsilon_1(\omega)$. On the other hand, $\varepsilon_2(\omega)$ provides data regarding the material performance in terms of the energy gain and absorption capacity.[64]

The dielectric function's real (ε_1) and imaginary (ε_2) values can be adjusted through the application of Kramer–Kronig equations.[18] Initially, we computed the real part (ε_1), as depicted in Fig. 5(a). Static dielectric function, or $\varepsilon_1(0)$, is the value of the real component (ε_1) at zero angular frequency. Using Penn's model, this $\varepsilon_1(0)$ illustrates the relationship with the band structure. Penn's model is confirmed by a maximum increase in the value of $\varepsilon_1(0)$ when the energy of the band gap (E_g) decreases.[65] A higher value of $\varepsilon_1(0)$ for Rb_2BiAuX_6 (X = Cl, Br, I) indicates a reduced charge recombination rate, which improves the photovoltaic device performance.

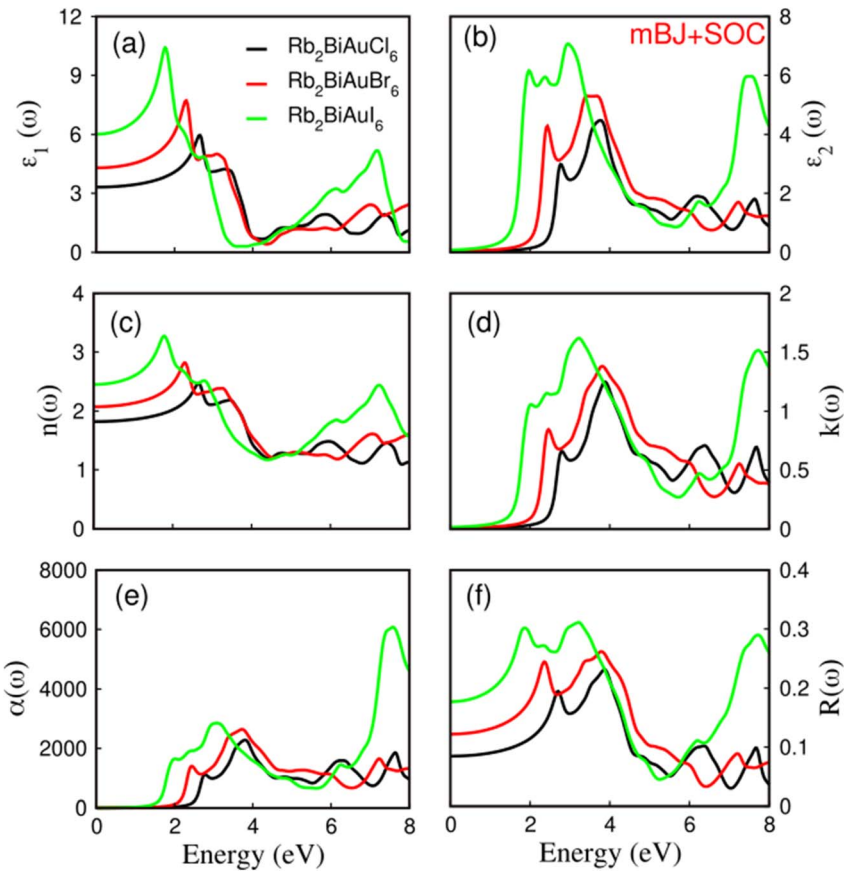

Fig. 5 The computed optical characteristics for Rb_2BiAuX_6 (X = Cl, Br, and I): (a) real part $\varepsilon_1(\omega)$ of the dielectric function, (b) imaginary part $\varepsilon_2(\omega)$ of the dielectric function, (c) the refractive index $n(\omega)$, (d) the extinction coefficient $k(\omega)$, (e) the absorption coefficient $\alpha(\omega)$, and (f) reflectivity $R(\omega)$ by employing mBJ + SOC.

At zero frequency limits, the $\varepsilon_1(\omega)$ is estimated to be 3.32, 4.47, and 6.26 for $Rb_2BiAuCl_6$, $Rb_2BiAuBr_6$, and Rb_2BiAuI_6, respectively. The compound produces slightly resonant frequencies, as evidenced by the maximum peak in the optical spectra for $Rb_2BiAuCl_6$ (5.75 at 2.5 eV), $Rb_2BiAuBr_6$ (7.86 at 2.0 eV), and Rb_2BiAuI_6 (10.61 at 1.5 eV). The $\varepsilon_2(\omega)$ defines the inter-band transition energy and absorption of the incoming photon within the energy range of 0–6 eV, as depicted in Fig. 5(b). The evaluated graphs indicate that for all studied materials, $\varepsilon_2(\omega)$ increases linearly beyond certain crucial points known as absorption edges, which may be accurately determined by projecting the linearly rising absorption to the energy axis. The values of the absorption edges correlate with the corresponding electronic energy gap, as seen in Fig. 4. The maximum value of the absorption is determined at 3.8 eV, 3.7 eV and 3.2 eV for $Rb_2BiAuCl_6$, $Rb_2BiAuBr_6$, and Rb_2BiAuI_6, respectively. The significant absorption peaks demonstrate a decrease in energy when the halogen anions switch from Cl to I, which is consistent with the computed energy gap. The maximum absorption peaks are positioned in the energy region (1.7–3.4 eV) for all studied materials, which is known as the visible energy region. According to the electromagnetic spectrum of the Sun, the radiations with energy less than 3.4 eV make up 98% of the solar system's energy that reaches Earth.[66] So, all three double perovskites have potential in the field of solar cell devices. Parameters like the extinction coefficient and refractive index were evaluated by using the following relation $n^2 - k^2 = \varepsilon_1(\omega)$, $2nk = \varepsilon_2(\omega)$.

The evaluated refractive index $n(\omega) = n(\omega) + ik(\omega)$, (here, $n(\omega)$ represents refractive index while $k(\omega)$ stands for extinction coefficient) as a function of angular frequency for $Rb_2BiAuCl_6$, $Rb_2BiAuBr_6$, and Rb_2BiAuI_6 is plotted in Fig. 5(c). The static $n(\omega)$ values for $Rb_2BiAuCl_6$, $Rb_2BiAuBr_6$, and Rb_2BiAuI_6 are computed to be 3.24, 4.43, and 6.21, respectively, which are higher than that for Rb_2AgPX_6 (X = Cl, Br, I)[1] and Rb_2AgSbX_6 (Cl, Br, I).[67] As the energy value increases, the magnitudes of $n(\omega)$ decreases. After exhibiting a minor peak, it ultimately becomes fractional, indicating the capability of Rb_2BiAuX_6 for superluminal applications. The $k(\omega)$ describes the material's potential to attenuate impinging photon.[68] Both imaginary parameter and $k(\omega)$ have the same response to the incident photon. The character of $k(\omega)$ with respect to the incident photon is depicted in Fig. 5(d). It shows that the absorption has the high value when the refractivity is lowered to its minimum value, making Rb_2BiAuX_6 opaque.

The absorption coefficient $\alpha(\omega)$ illustrates how much energy is needed for each unit of distance as light decays. High $\alpha(\omega)$ values are observed at 3.8 eV, 3.76 eV and 2.85 eV for $Rb_2BiAuCl_6$ (2100 m^{-1}), $Rb_2BiAuBr_6$ (2400 m^{-1}) and Rb_2BiAuI_6 (2800 m^{-1}), respectively, as illustrated in Fig. 5(e). These values are comparable with that for Rb_2LiTlX_6 (X = Cl, Br).[69] The absorption coefficient ($\alpha(\omega)$) values increase with decreasing bandgap. Reflectivity ($R(\omega)$) is an important factor of optical properties that provides information about the surface roughness of the studied compound.[70–72] It has been seen in Fig. 5(f) that the $R(\omega)$ of the studied double perovskite material rises significantly as the halogen anion is changed from Cl^- to I^-. However, the comparatively minimum $R(\omega)$ in the visible spectrum illustrates the possibility of using Rb_2BiAuX_6 in solar cell applications. Additionally, the maximum $R(\omega)$ of Rb_2BiAuX_6 in the UV regions suggests the compound application in coatings to reduce the heating effect.

3.5. Thermoelectric properties

Another effective strategy for satisfying the world's energy needs is to transform thermal energy into electrical energy. Consequently, in the area of energy requirements, the study of electronic transport properties is crucial. To determine the thermoelectric parameter values, the BoltzTrap code is utilized.[73] Fig. 5 shows the essential characteristics that are determined *versus* temperature from low (100 K) to high (800 K) values. These include the electronic thermal conductivity (k_e/τ), electrical conductivity (σ/τ) (as 'τ' represents the relaxation time), power factor (PF) (each standardized by the value of 'τ'), Seebeck coefficient S, and power factor (PF). The compound's thermal behavior can be explained by their high power factor and figure of merits. These characteristics can only be achieved when the thermal conductivity plays a relatively minor role, and the electrical conduction and Seebeck coefficient are high.

From Fig. 6(a), it can be seen that the electrical conductivity (σ/τ) for Rb_2BiAuX_6 (X = Cl, Br, I) increases with increasing temperature. Values such as 0.18×10^{19} $(\Omega\ ms)^{-1}$, 0.21×10^{19} $(\Omega\ ms)^{-1}$ and 0.26×10^{19} $(\Omega\ ms)^{-1}$ are calculated for $Rb_2BiAuCl_6$, $Rb_2BiAuCl_6$, and $Rb_2BiAuCl_6$, respectively. Interestingly, these values increase with increasing temperature, which clearly shows the increasing interaction of electrons with temperature. Another crucial parameter is the Seebeck coefficient (S), which describes the electric potential across a material's edges caused by temperature gradients $S = \Delta V/\Delta T$.[74] The estimated values of S for $Rb_2BiAuCl_6$, $Rb_2BiAuBr_6$, and Rb_2BiAuI_6 are 242 μV K^{-1}, 240 μV K^{-1}, and 223 μV K^{-1} at temperature (300 K), respectively, as shown in Fig. 6(b). As the temperature gets closer to 800 K, the values of S decrease because more thermally excited carriers are present. Because the additional carriers dilute the voltage response per temperature gradient, they can lead to a decreased Seebeck coefficient, which in turn lowers S.

An extremely low thermal-to-electrical conductivity ratio is desirable in a thermoelectric material, according to research on thermal conductivity (k_e/τ). This property suggests that the material being studied may be suitable for use as a thermoelectric material. The electronic thermal conductivity (k_e/τ) for $Rb_2BiAuCl_6$ is 0.50×10^{14} W m^{-1} K^{-1} s^{-1} at 300 K and rises to 4.055×10^{14} W m^{-1} K^{-1} s^{-1} at 800 K. For $Rb_2BiAuBr_6$, it is 0.45×10^{14} W m^{-1} K^{-1} s^{-1} at 300 K and rises to 4.45×10^{14} W m^{-1} K^{-1} s^{-1} at 800 K. Lastly, the calculated value for Rb_2BiAuI_6 is 0.6136×10^{14} W $(m\ K\ s)^{-1}$ at room temperature and rises with temperature to 4.48×10^{14} W m^{-1} K^{-1} s^{-1} at 800 K, as depicted in Fig. 6(c). A lower thermal conductivity is typically valued for an effective thermoelectric material.

Heat capacity (C_v) is the amount of heat energy, measured in joules or calories, that an electronic device can store. Temperature increases are typically accompanied by increases in heat

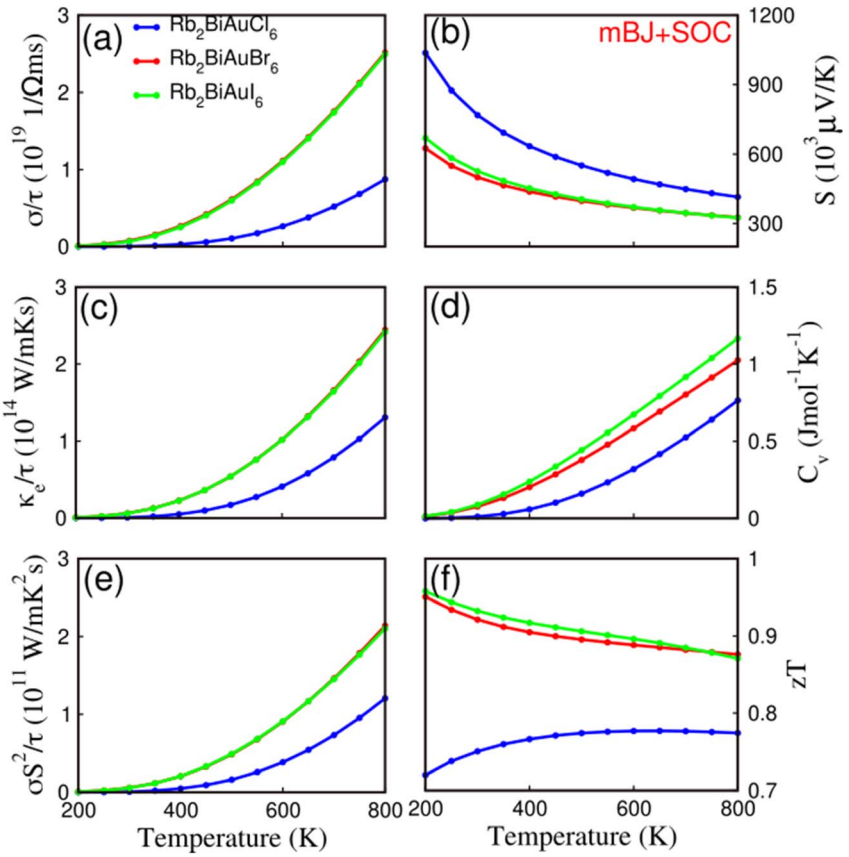

Fig. 6 The computed thermoelectric characteristics for Rb_2BiAuX_6 (X = Cl, Br, and I): (a) electrical conductivity, (b) Seebeck coefficient, (c) thermal conductivity, (d) heat capacity, (e) power factor and (f) figure of merit by employing mBJ + SOC.

capacity. This is not the case unless the system (device) turns into a gas, vapor, or melts from a solid to a liquid. The harmonic approximation is nearly always accurate at low temperatures because the vibration's amplitude decreases.[75] The specific heat capacity of different material states is often influenced by temperature. The melting of the extra degrees of freedom with increasing temperature (seen in Fig. 6(d)) causes the value of (C_v) for Rb_2BiAuX_6 (X = Cl, Br, I) to increase.

Since the power factor measures how effectively thermoelectric materials transfer thermal into electrical power, it is essential to calculate it while assessing them. The formula for the power factor (PF) is $PF = \sigma S^2$, where σ is the electrical conductivity and S is the Seebeck coefficient.[76] As the temperature increases from 300 K to 800 K, the power factor for $Rb_2BiAuCl_6$ increases from 0.38 × 10^{11} (W m^{-1} K^{-2} s^{-1}) to 3.15 × 1011 (W m^{-1} K^{-}2 s^{-1}). For $Rb_2BiAuBr_6$, it increases from 0.33 × 10^{11} (W m^{-1} K^{-2} s^{-1}) to 3.27 × 10^{11} (W m^{-1} K^{-2} s^{-1}). Meanwhile, for Rb_2BiAuI_6, it increases from 0.44 × 10^{11} (W m^{-1} K^{-2} s^{-1}) to 3.36 × 10^{11} (W m^{-1} K^{-2} s^{-1}), seen in Fig. 6(e). The power factor is an acute component that affects the economic feasibility and effectiveness of thermoelectric materials and devices during development and usage.[77,78] The dimensionless quantity figure of merit ($ZT = S^2\sigma T/K$) is an important statistic that may help us understand how to increase the material performance with temperature fluctuation. A high thermoelectric figure of merit corresponds to a thermoelectric material that is very efficient. ZT depends on the electrical conductivity, thermal conductivity, and a high Seebeck coefficient.[36,37] Thus, the calculated ZT values of $Rb_2BiAuCl_6$, $Rb_2BiAuBr_6$ and Rb_2BiAuI_6 are 0.76, 0.75 and 0.77, respectively, at room temperature. It should be noted that we have also checked the k-point dependence on the thermoelectric properties. We have observed a negligible variation in the thermoelectric properties with increasing k-points.

Additionally, the Phono3py[26] code is used to calculate the total lattice thermal conductivity (k_l). We followed ref. 79 and 80 to compute the k_l. The computed thermal conductivities attributed to the phononic (k_l) processes across the temperature range of 0–1000 K is shown in Fig. 7. The declining trend has been observed for k_l with increasing temperature. The values of lattice conductivity k_l at room temperature are 0.07 W K^{-1} m^{-1}, 0.02 W K^{-1} m^{-1} and 0.007 W K^{-1} m^{-1} for $Rb_2BiAuCl_6$, $Rb_2BiAuBr_6$ and Rb_2BiAuI_6, respectively, which are comparable to those of Cs_2BiAgX_6 (0.078 W K^{-1} m^{-1} to 0.065 W K^{-1} m^{-1}) and many more.[81,82]

The BoltzTraP source code computes the transport characteristics and describes the Fermi-unification and carrier concentrations. In Fig. 8, the transport parameters are shown against the chemical potential. The positive and negative values for the n-type and p-type sites, respectively, represent the energy

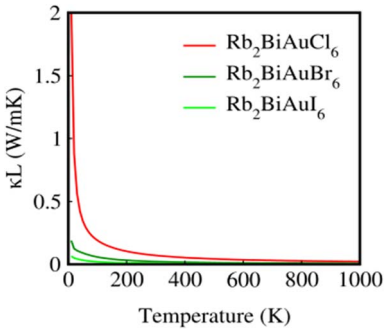

Fig. 7 The computed lattice thermal conductivity for Rb_2BiAuX_6 (X = Cl, Br, and I).

required to move both electrons and holes in the direction of the incoming potential. The number of electrons and holes present for conduction is measured by electrical conductivity (σ/τ).[83] The compounds under investigation satisfy the ideal thermoelectric compound's criteria of having very low thermal-to-electrical conductivity.[83] Fig. 8(a) shows the trend of σ/τ for $Rb_2BiAuCl_6$, $Rb_2BiAuBr_6$, and Rb_2BiAuI_6 against a chemical potential range of -2 eV to 3 eV. The highest peaks for the p-type are calculated as 0.96×10^{19} (1/Ω ms), 1.47×10^{19} (1/Ω ms) and 1.48×10^{19} (1/Ω ms) for $Rb_2BiAuCl_6$, $Rb_2BiAuBr_6$, and Rb_2BiAuI_6, respectively, which indicates the maximum presence of hole carriers for $Rb_2BiAuBr_6$ and Rb_2BiAuI_6. The maximum values of hole carriers for $Rb_2BiAuBr_6$ and Rb_2BiAuI_6 may be due to the large ionic radii of Br and I atoms. Furthermore, the carriers in the n-type side start at 1.8 eV, 1.2 eV and 0.7 eV for $Rb_2BiAuCl_6$, $Rb_2BiAuBr_6$, and Rb_2BiAuI_6, respectively. The peak values are found to be 1.04×10^{19} (1/Ω ms), 2.02×10^{19} (1/Ω ms) and 2.23×10^{19} (1/Ω ms) for $Rb_2BiAuCl_6$, $Rb_2BiAuBr_6$, and Rb_2BiAuI_6, respectively. This increase in the n-type side carriers are due to the higher density of states near CBM and a light effective mass of electrons.

A key thermoelectric parameter that is computed throughout a range of chemical potential, the Seebeck coefficient (S) shows the potential difference with the temperature gradient ratio.[84] The S plot against the chemical potential range of 2 eV to 3 eV is depicted in Fig. 8(b). Near the Fermi energy ($\mu = 0$), the S is +ve, suggesting that hole carriers dominate. At higher or lower μ, S becomes $-$ve, showing that electron carriers dominate when the Fermi level shifts into conduction bands. Moreover, the S has revealed maximum peaks on the p-type side because σ/τ has higher values for electron carriers. At 300 K, the magnitudes of S are 2.7×10^3 μV K^{-1}, 1.8×10^3 μV K^{-1}, and 1.06×10^3 μV K^{-1} for $Rb_2BiAuCl_6$, $Rb_2BiAuBr_6$, and Rb_2BiAuI_6, respectively. The material efficiency of thermal devices is determined by the figure of merit (ZT). The ZT plot against the chemical potential is represented in Fig. 8(c). On the negative chemical potential (hole side), $Rb_2BiAuCl_6$ has the maximum value of ZT because it has lower σ/τ and the higher S value for hole carriers, so ZT stays high. This behavior of $Rb_2BiAuCl_6$ shows that the material is p-type favorable. On the positive chemical potential (electron side), $Rb_2BiAuBr_6$ and Rb_2BiAuI_6 have maximum values of ZT, reaching near unity. So, $Rb_2BiAuBr_6$ and Rb_2BiAuI_6 are n-type favorable materials. Moreover, the plots of ZT against the μ carrier concentration for both n-type and p-type sides approximately reach near unity, indicating the potential of these studied materials for a thermoelectrical device. Our results for the chemical potential are comparable with that of the recently investigated double perovskite materials Rb_2AgPX_6 (X = Cl, Br, I).[1]

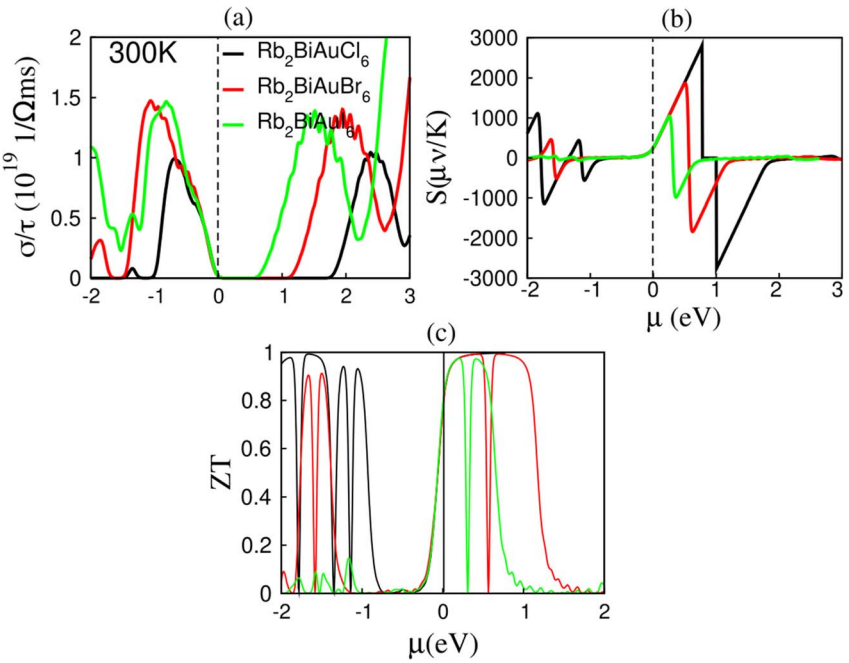

Fig. 8 The computed thermoelectric characteristics for Rb_2BiAuX_6 (X = Cl, Br, and I): (a) electrical conductivity, (b) Seebeck coefficient and (c) figure of merit against chemical potential by employing mBJ + SOC.

Moreover, thermoelectric properties such as the electrical conductivity, Seebeck coefficient and figure of merit against the carrier concentration (N (e/uc)) with the positive and negative doping of all studied materials were calculated, as shown in Fig. 9. Fig. 9(a) shows the response of σ/τ for $Rb_2BiAuCl_6$, $Rb_2BiAuBr_6$, and Rb_2BiAuI_6 *versus* the carrier concentration from −3 eV to 4 eV. The maximum values of the electrical conductivity for p-type are calculated as 17.93×10^{19} (1/Ω ms), 21.67×10^{19} (1/Ω ms) and 18.48×10^{19} (1/Ω ms) at $-3.0N$ (e/uc) for $Rb_2BiAuCl_6$, $Rb_2BiAuBr_6$, and Rb_2BiAuI_6, respectively, which indicates the maximum presence of hole carrier concentrations for $Rb_2BiAuBr_6$ and Rb_2BiAuI_6. However, for n-type, the peak values are found to be 11.99×10^{19} (1/Ω ms), 15.18×10^{19} (1/Ω ms) and 13.97×10^{19} (1/Ω ms) for $Rb_2BiAuCl_6$, $Rb_2BiAuBr_6$, and Rb_2BiAuI_6, respectively. Overall, the maximum electrical conductivity values for $Rb_2BiAuBr_6$ in both doping types are due to its more favorable electronic structure, with optimized band dispersion and improved carrier mobility (as shown in Table 1).

The S plot against the carrier concentration (N (e/uc)) in the range of −3 eV to 4 eV is depicted in Fig. 9(b). The most common behavior observed is that the S falls with increasing carrier concentration, which is typical for semiconducting compounds. This inverse relationship arises because a maximum N (e/uc) increases the electrical conductivity, but decreases the thermoelectric voltage generated per unit temperature gradient. As shown in Fig. 9(b), it is clear that $Rb_2BiAuCl_6$ exhibits slightly higher Seebeck coefficients than the Br and I analogs, particularly at lower N value. This indicates that $Rb_2BiAuCl_6$ has a larger effective mass or a more favorable band structure near the Fermi level, enhancing the thermopower.

Fig. 9(c) shows that for all materials under study, the ZT values at $0N$ (e/uc) are unity (1). However, the ZT values sharply fall with increasing p-type doping and linearly decrease with increasing n-type doping. Our carrier concentration results are comparable with that of the recently investigated double perovskite material A_2YAuI_6 (A = Rb, Cs).[85]

3.6. Thermodynamic properties

Thermodynamic properties are important for finding the quantities of heat energy needed to alter the temperature of the compound and the quantity of work needed to cause the material to expand or contract.[86] The thermodynamic characteristics of Rb_2BiAuX_6 (X = Cl, Br, I) are calculated by employing the quasi-harmonic Debye model[32,87] within the temperature range of 0 K to 800 K and pressure range of 0 GPa to 4 GPa. Various thermodynamic parameters, such as the adiabatic bulk modulus, Helmholtz free energy, specific heat capacity, Debye temperature and Gibbs free energy, have been examined for the investigated compounds under varying pressures and temperatures.

The resistance of a material to deformation under adiabatic conditions (without heat exchange) is quantified by its adiabatic bulk modulus. The adiabatic bulk modulus values for $Rb_2BiAuCl_6$, $Rb_2BiAuBr_6$, and Rb_2BiAuI_6 are plotted in Fig. 10(a). At 0 K and 4 GPa pressure, the value of the adiabatic bulk modulus

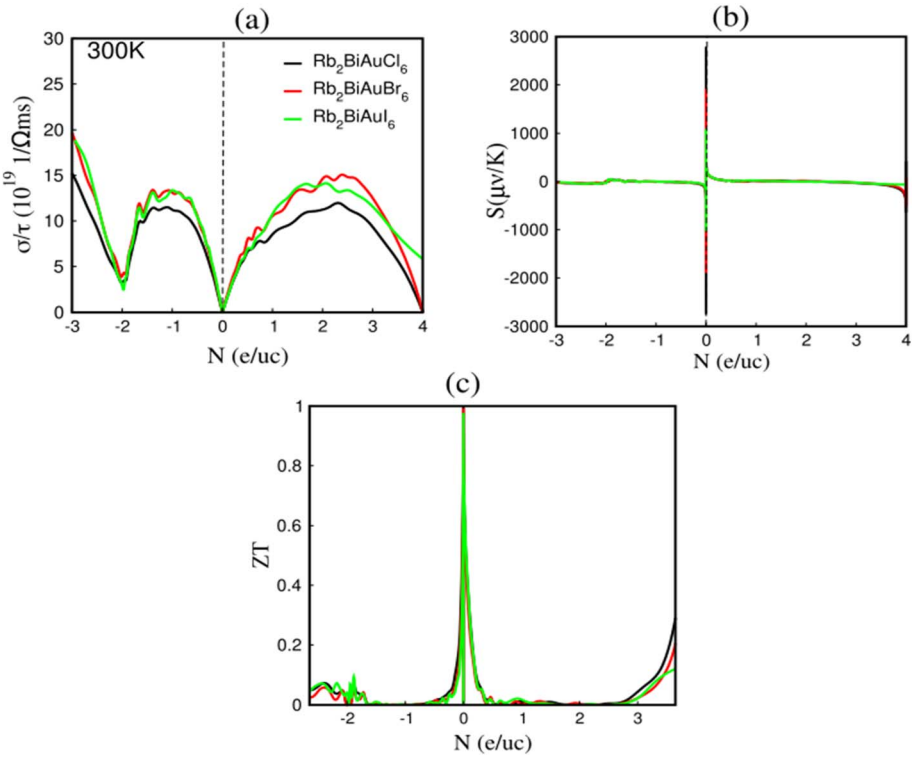

Fig. 9 The computed thermoelectric characteristics for Rb_2BiAuX_6 (X = Cl, Br, I): (a) electrical conductivity, (b) See-beck coefficient and (c) figure of merit against the carrier concentration (N) by employing mBJ + SOC.

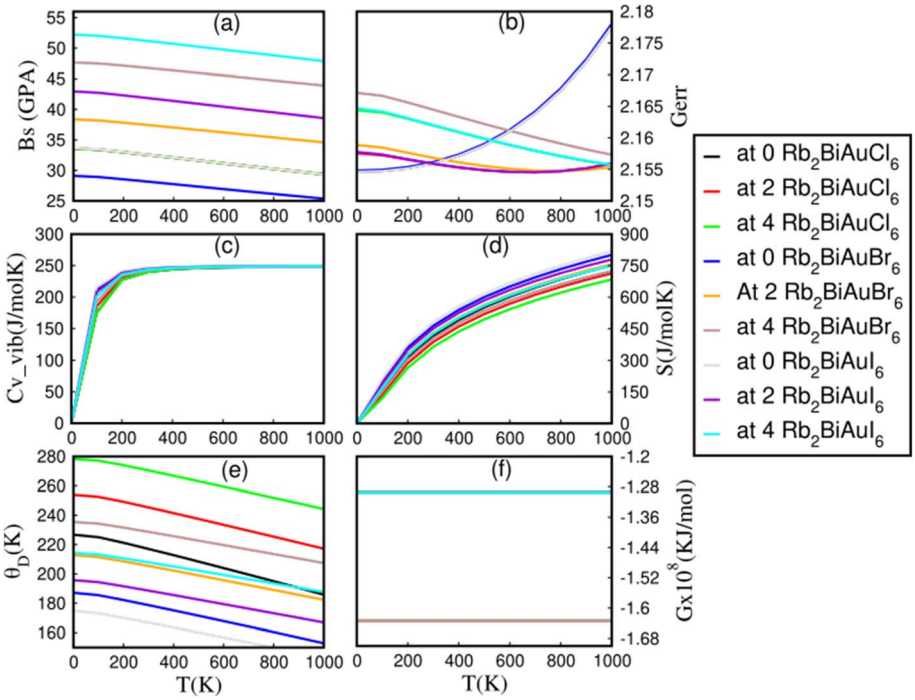

Fig. 10 Thermodynamic properties of Rb_2BiAuX_6 with respect to temperature (K): (a) adiabatic bulk modulus, (b) Helmholtz free energy, (c) specific heat capacity, (d) entropy, (e) Debye temperature and (f) Gibbs free energy by employing mBJ + SOC.

for Rb_2BiABr_6 rises to 48 GPa, from 29 GPa at 0 K and 0 GPa pressure to 39 GPa at 0 K and 2 GPa. Similarly, in the case of Rb_2BiAuI_6, at 0 K and 4 GPa pressure, the value of the adiabatic bulk modulus rises to 52 GPa, from 34 GPa at 0 K and 0 GPa pressure to 43 GPa at 0 K and 2 GPa. The adiabatic bulk moduli for $Rb_2BiAuBr_6$ and Rb_2BiAuI_6 increased with the implementation of pressure, suggesting that these compounds become stronger under compression. However, when we incorporate the Cl atom at the X-site, the results of the adiabatic bulk modulus are quite different than that of $Rb_2BiAuBr_6$ and Rb_2BiAuI_6. The calculated value of the adiabatic bulk modulus for $Rb_2BiAuCl_6$ is found to be 33 GPa at 0 K, which is almost constant at all pressure values. The reason is that Cl is more electronegative and less polarizable than Br/I, so the Au–Cl/Bi–Cl bonding is stronger (shorter, stiffer bonds). Stiffer bonds cause higher lattice thermal conductivity. As a result, there is a smaller thermal response under compression. The bulk modulus, conversely, decreases with temperature, indicating that the compounds diminish in their resistance to compression. This is a common behaviour since elevated temperatures generally lead to a rise in atomic vibrations, resulting in a reduction of the material's stiffness.

As illustrated in Fig. 10(b), the Helmholtz free energies for $Rb_2BiAuCl_6$, $Rb_2BiAuBr_6$, and Rb_2BiAuI_6 show very unique behaviour under different pressures and temperatures. Due to the absence of thermal entropy, the Helmholtz energy reaches its maximum at 0 GPa and 0 K. The Helmholtz energy for Rb_2BiAuX_6 decreases as the temperature rises from 0 K to 200 K at 0 GPa due to the *TS* (temperature–entropy) factor reducing the internal energy of the system. The Helmholtz energy increases above 200 K at 0 GPa, which may be due to a phase transition. The Helmholtz free energy values for all studied materials are directly related to the pressure. As the pressure increases from 0 GPa to 4 GPa, the Helmholtz energy of Rb_2BiAuX_6 also rises significantly at 0 K, indicating how much pressure affects the entropy and internal energy of the compounds.

As the pressure and temperature rise, the vibrational component of the constant volume heat capacity (C_v) increases. Fig. 10(c) exhibits the response of C_v for $Rb_2BiAuCl_6$, $Rb_2BiAuBr_6$, and Rb_2BiAuI_6 as a function of temperature and pressure. The C_v corresponds to the Dulong–Petit limit at higher temperatures and conforms to the T^3 (ref. 88) law at reduced temperatures. This trend is a defining property of materials at low temperatures, indicating the quantum mechanical origin of C_v, especially at these circumstances. In contrast, at elevated temperatures, the specific heat capacity is more likely to agree with the Dulong–Petit limit. This limit signifies a saturation point, beyond which the specific heat capacity does not demonstrate significant increases with temperature. This shows that the system has attained a condition of thermal energy equilibrium. However, when we enhance the pressure, the atoms of the material come closer to each other. As a result, the vibrational frequencies and heat capacity change, while the maximum value of the temperature induces additional vibrational modes. Consequently, these constituents enhance the material's ability to absorb and transfer thermal energy.

Entropy, an indicator of disorder inside a system, is a basic thermodynamic phenomenon, and its response is of significant importance.[89] The entropy for $Rb_2BiAuCl_6$, $Rb_2BiAuBr_6$, and

Rb_2BiAuI_6 increases almost linearly with pressure and temperature, as shown in Fig. 10(d). Entropy starts from zero at 0 K, reflecting the lack of thermal energy. The finding is consistent with recognised thermodynamic concepts.[90] However, when the temperature increases, mostly owing to thermal vibrations, the system's entropy also increases. Likewise, atoms or molecules are subjected to compression under elevated pressure, which under some circumstances may similarly induce disorder and result in a linear escalation in entropy. This linear relationship indicates that the entropy of the materials is directly and proportionally affected by both pressure and temperature, reflecting a steady increase in the system's disorder and thermal energy distribution. This discernible tendency is a primary finding of our study. The determined relative entropy values for the different compounds under investigation are noteworthy.

Fig. 10(e) represents the variations of the Debye temperature (θ_D) for $Rb_2BiAuCl_6$, $Rb_2BiAuBr_6$, and Rb_2BiAuI_6. θ_D is a crucial parameter that denotes the shift to a classical trend in a crystal. It offers significant insights into the material characteristics, including the specific heat capacity. From the plot, it can be observed that θ_D has an inverse relationship with temperature for all studied materials because θ_D decreases as we increase the temperature value from 0 K to 800 K. This behaviour indicates that as the temperature rises, the vibrational modes of the crystal show increasing frequency, resulting in lower total energy and a typical θ_D. On the other hand, the Debye temperature has a direct relationship with pressure because θ_D rises significantly as we increase the pressure. These thermodynamic findings provide a basis for further study on $Rb_2BiAuCl_6$, $Rb_2BiAuBr_6$, and Rb_2BiAuI_6, facilitating the comprehension of their material characteristics and behaviour under varying situations. The θ_D provides insights into the system's vibrational and thermal properties, aiding researchers in predicting and analysing phenomena such as entropy, lattice dynamics, and specific heat capacity.

The Gibbs free energy values for $Rb_2BiAuCl_6$, $Rb_2BiAuBr_6$, and Rb_2BiAuI_6 as a function of pressure and temperature are plotted in Fig. 10(f). It has been observed that the Gibbs free energy values for $Rb_2BiAuCl_6$, $Rb_2BiAuBr_6$, and Rb_2BiAuI_6 have constant values of -1.29×10^8 kJ mol^{-1}, 1.67×10^8 kJ mol^{-1} and -1.29×10^8 kJ mol^{-1}, respectively, at all pressures and temperatures. This stability indicates that the relationship between the enthalpy and entropy is stable, since it demonstrates that the Gibbs free energy exhibits little fluctuation in response to changes in the temperature and pressure. In other words, the alterations in entropy mitigate the variations in the internal energy associated with pressure and temperature, resulting in a relatively stable Gibbs free energy. This trend indicates an equilibrium framework, signifying that the total Gibbs free energy stays generally stable throughout the examined conditions owing to the appropriate contributions from thermal and pressure-induced operations.

4. Summary

In conclusion, we have studied the structural, mechanical, optoelectronic, and thermal characteristics of Rb_2BiAuX_6 (X = Cl, Br, I) using first-principles calculations. Our findings reveal that $Rb_2BiAuCl_6$ is the most energetically favorable among the three materials due to the lowest formation energy. All Rb_2BiAuX_6 compounds are mechanically stable, as indicated by their high elastic constants. These materials display semiconducting behavior, with band gaps ranging from 0.61 to 1.8 eV. The optical characteristics, characterized by strong absorption peaks, suggest that they are promising candidates for solar cell applications. Furthermore, $Rb_2BiAuCl_6$ exhibits the highest thermoelectric figure of merit ($ZT = 0.78$ at 300 K) among the materials studied. These results suggest that the Rb_2BiAuX_6 compounds have significant promising potential for application in thermal energy systems, as well as solar energy cells.

Conflicts of interest

The authors declare that they have no known competing financial interests.

Data availability

The data used in this study can be made available on a reasonable request from the corresponding author.

Acknowledgements

J. T. Wang acknowledges the financial support from the National Natural Science Foundation of China (Grant No. 92263202 and No. 12374020), the National Key Research and Development Program of China (Grant No. 2020YFA0711502), and the Strategic Priority Research Program of the Chinese Academy of Sciences (Grant No. XDB33000000). Authors also acknowledge Princess Nourah bint Abdulrahman University Researchers Supporting Project number (PNURSP2025R398), Princess Nourah bint Abdulrahman University, Riyadh, Saudi Arabia.

References

1 F. Ali, M. Asghar, H. S. Waheed, H. Ullah, M. J. I. Khan, G. Anwar, M. Amin, S. M. Wabaidur and Y.-H. Shin, *Opt. Quantum Electron.*, 2024, **56**, 1094.
2 Q. A. Akkerman, M. Gandini, F. Di Stasio, P. Rastogi, F. Palazon, G. Bertoni, J. M. Ball, M. Prato, A. Petrozza and L. Manna, *Nat. Energy*, 2016, **2**, 1–7.
3 I. A. Ajia, P. R. Edwards, Z. Liu, J. C. Yan, R. W. Martin and I. S. Roqan, *Appl. Phys. Lett.*, 2014, **105**, 122111.
4 B. Liu, M. Köpf, A. N. Abbas, X. Wang, Q. Guo, Y. Jia, F. Xia, R. Weihrich, F. Bachhuber, F. Pielnhofer, H. Wang, R. Dhall, S. B. Cronin, M. Ge, X. Fang, T. Nilges and C. Zhou, *Adv. Mater.*, 2015, **27**, 4423–4429.
5 S. Alnujaim, A. Bouhemadou, A. Bedjaoui, S. Bin-Omran, Y. Al-Douri, R. Khenata and S. Maabed, *J. Alloys Compd.*, 2020, **843**, 155991.

6 C. W. Ahn, J. H. Jo, J. Chan Kim, H. Ullah, S. Ryu, Y. Hwang, J. San Choi, J. Lee, S. Lee, H. Jeen, Y.-H. Shin, H. Y. Jeong, I. W. Kim and T. H. Kim, *J. Materiomics*, 2020, **6**, 651–660.
7 M. A. Amin, G. Nazir, Q. Mahmood, J. Alzahrani, N. A. Kattan, A. Mera, H. Mirza, A. Mezni, M. S. Refat, A. A. Gobouri and T. Altalhi, *J. Mater. Res. Technol.*, 2022, **18**, 4403–4412.
8 M. Hussain, F. Ali, H. Ullah, S. Tehreem Iqbal, F. Anjum, M. A. El-Sheikh and Y.-H. Shin, *J. Magn. Magn. Mater.*, 2024, **598**, 172055.
9 M. Asghar, H. S. Waheed, U. Abbas, H. Ullah, M. J. I. Khan, S. M. Wabaidur, A. Ali and Y.-H. Shin, *Phys. B*, 2024, **682**, 415916.
10 D. C. Arnold, K. S. Knight, G. Catalan, S. A. T. Redfern, J. F. Scott, P. Lightfoot and F. D. Morrison, *Adv. Funct. Mater.*, 2010, **20**, 2116.
11 H. J. Snaith, *Adv. Funct. Mater.*, 2010, **20**, 13–19.
12 B. Li, H. Wang, Y. Kawakita, Q. Zhang, M. Feygenson, H. L. Yu, D. Wu, K. Ohara, T. Kikuchi, K. Shibata, T. Yamada, X. K. Ning, Y. Chen, J. Q. He, D. Vaknin, R. Q. Wu, K. Nakajima and M. G. Kanatzidis, *Nat. Mater.*, 2018, **17**, 226–230.
13 E. D. L. Rienks, S. Wimmer, J. Sánchez-Barriga, O. Caha, P. S. Mandal, J. Růžička, A. Ney, H. Steiner, V. V. Volobuev, H. Groiss, M. Albu, G. Kothleitner, J. Michalička, S. A. Khan, J. Minár, H. Ebert, G. Bauer, F. Freyse, A. Varykhalov, O. Rader and G. Springholz, *Nature*, 2019, **576**, 423–428.
14 J. Muscat, A. Wander and N. M. Harrison, *Chem. Phys. Lett.*, 2001, **342**, 397–401.
15 K. Assiouan, A. Marjaoui, J. EL Khamkhami, M. Zanouni, H. Ziani, A. Bouchrit and A. Achahbar, *J. Phys. Chem. Solids*, 2024, **188**, 111890.
16 M. Basit Shakir, G. Murtaza, A. Ayyaz, M. Touqir, H. Khan, A. Akremi, H. Irfan Ali, A. Usman, A. S. Altowyan and K. Iqbal, *Mater. Sci. Eng., B*, 2024, **310**, 117667.
17 N. P. Mathew, N. Rajeev Kumar and R. Radhakrishnan, *Mater. Today: Proc.*, 2020, **33**, 1252–1256.
18 G. M. Mustafa, B. Younas, A. Ayyaz, A. I. Aljameel, S. Alotaibi, S. Bouzgarrou, S. K. Ali, Q. Mahmood, I. Boukhris and M. S. Al-Buriahi, *RSC Adv.*, 2025, **15**, 5202–5213.
19 A. Ayyaz, M. Zaman, H. D. Alkhaldi, H. I. Ali, I. Boukhris, S. Bouzgarrou, M. mana Al-Anazy and Q. Mahmood, *RSC Adv.*, 2025, **15**, 11128–11145.
20 H. I. Ali, A. Ayyaz, N. D. Alkhaldi, I. Boukhris, M. S. Al-Buriahi, Q. Mahmood, T. Alshahrani and S. Bouzgarrou, *Inorg. Chem. Commun.*, 2025, **176**, 114301.
21 M. Yaseen, H. Ambreen, J. Iqbal, A. Shahzad, R. Zahid, N. A. Kattan, S. M. Ramay and A. Mahmood, *Philos. Mag.*, 2020, **100**, 3125–3140.
22 D. Bouhafs, A. Moussi, A. Chikouche and J. M. Ruiz, *Sol. Energy Mater. Sol. Cells*, 1998, **52**, 79–93.
23 Y. H. Hou, Y. J. Zhao, Z. W. Liu, H. Y. Yu, X. C. Zhong, W. Q. Qiu, D. C. Zeng and L. S. Wen, *J. Phys. D:Appl. Phys.*, 2010, **43**, 445003.
24 J. P. Perdew, A. Ruzsinszky, G. I. Csonka, O. A. Vydrov, G. E. Scuseria, L. A. Constantin, X. Zhou and K. Burke, *Phys. Rev. Lett.*, 2008, **100**, 136406.
25 A. D. Becke and E. R. Johnson, *J. Chem. Phys.*, 2006, **124**, 221101.
26 A. Togo, L. Chaput and I. Tanaka, *Phys. Rev. B*, 2015, **91**, 094306.
27 J. Hafner, *J. Comput. Chem.*, 2008, **29**, 2044–2078.
28 G. Kresse and J. Furthmüller, *Comput. Mater. Sci.*, 1996, **6**, 15–50.
29 S. Nosé, *J. Chem. Phys.*, 1984, **81**, 511–519.
30 Y. C. Cheng, Z. Y. Zhu, W. B. Mi, Z. B. Guo and U. Schwingenschlögl, *Phys. Rev. B*, 2013, **87**, 100401.
31 P. Lallemand and L.-S. Luo, *Phys. Rev. E:Stat., Nonlinear, Soft Matter Phys.*, 2003, **68**, 036706.
32 A. Otero-de-la-Roza, D. Abbasi-Pérez and V. Luaña, *Comput. Phys. Commun.*, 2011, **182**, 2232–2248.
33 G. Anwar, Z. Iqbal, H. Ullah, W. Zulfiqar, M. Majid Gulzar and E. A. Al-Ammar, *Phys. B*, 2025, **701**, 416975.
34 L. Chu, W. Ahmad, W. Liu, J. Yang, R. Zhang, Y. Sun, J. Yang and X. Li, *Nano-Micro Lett.*, 2019, **11**, 16.
35 H. Murtaza, Q. Ain, J. Munir, H. Ullah, H. M. Ghaithan, A. A. Ali Ahmed and S. M. H. Qaid, *Sol. Energy*, 2024, **273**, 112502.
36 F. Aslam, H. Ullah and M. Hassan, *Phys. Scr.*, 2022, **97**, 045801.
37 F. Aslam, H. Ullah and M. Hassan, *Mater. Sci. Eng., B*, 2021, **274**, 115456.
38 H. S. Waheed, M. Asghar, H. S. Ahmad, T. Abbas, H. Ullah, R. Ali, M. J. I. Khan, M. W. Iqbal, Y.-H. Shin, M. S. Khan and R. Neffati, *Phys. Status Solidi B*, 2022, **260**, 2200267.
39 F. Mouhat and F.-X. Coudert, *Phys. Rev. B*, 2014, **90**, 224104.
40 R. Hill, *Proc. Phys. Soc., London, Sect. A*, 1952, **65**, 349.
41 G. K. Arusei, M. Chepkoech, G. O. Amolo and N. Wambua, *Comput. Condens. Matter*, 2024, **39**, e00891.
42 H. H. Raza, G. Murtaza, S. Razzaq and A. Azam, *Mol. Simul.*, 2023, **49**, 497–508.
43 H. H. Raza, G. Murtaza, M. Shafiq and S. Abdul Shakoor, *Int. J. Hydrogen Energy*, 2024, **62**, 637–651.
44 H. H. Raza, G. Murtaza, Z. Abbas, S. Razzaq, S. M. Ramay and M. Irfan, *Mater. Sci. Eng., B*, 2024, **300**, 117072.
45 C.-X. Li, Y.-H. Duan and W.-C. Hu, *J. Alloys Compd.*, 2015, **619**, 66–77.
46 M. Bilal, M. Shafiq, B. Khan, H. A. R. Aliabad, S. J. Asadabadi, R. Ahmad and I. Ahmad, *Phys. Lett. A*, 2015, **379**, 206–210.
47 N. A. Noor, M. Rashid, G. M. Mustafa, M. I. Khan, A. Mahmood and S. M. Ramay, *Chem. Phys. Lett.*, 2020, **753**, 137601.
48 W. Shockley and H. J. Queisser, *J. Appl. Phys.*, 1961, **32**, 510–519.
49 T. T. Tran, J. R. Panella, J. R. Chamorro, J. R. Morey and T. M. McQueen, *Mater. Horiz.*, 2017, **4**, 688–693.
50 Y. Pei, X. Shi, A. LaLonde, H. Wang, L. Chen and G. J. Snyder, *Nature*, 2011, **473**, 66–69.
51 Z. Xiao and Y. Yan, *Adv. Energy Mater.*, 2017, **7**, 1701136.
52 A. Ayyaz, G. Murtaza, A. Usman, N. Sfina, A. S. Alshomrany, S. Younus, S. Saleem and Urwa-tul-Aysha, *J. Inorg. Organomet. Polym. Mater.*, 2024, **34**, 3560–3575.
53 Y. Wang, Y. Zhang, P. Zhang and W. Zhang, *Phys. Chem. Chem. Phys.*, 2015, **17**, 11516–11520.

54 L.-J. Wu, Y.-Q. Zhao, C.-W. Chen, L.-Z. Wang, B. Liu and M.-Q. Cai, *Chin. Phys. B*, 2016, **25**, 107202.
55 C. Katan, N. Mercier and J. Even, *Chem. Rev.*, 2019, **119**, 3140–3192.
56 M. Bokdam, J. Lahnsteiner, B. Ramberger, T. Schäfer and G. Kresse, *Phys. Rev. Lett.*, 2017, **119**, 145501.
57 K. E. Babu, A. Veeraiah, D. T. Swamy and V. Veeraiah, *Chin. Phys. Lett.*, 2012, **29**, 117102.
58 M. Rashid, N. A. Noor, B. Sabir, S. Ali, M. Sajjad, F. Hussain, N. U. Khan, B. Amin and R. Khenata, *Comput. Mater. Sci.*, 2014, **91**, 285–291.
59 M. Hassan, A. Shahid and Q. Mahmood, *Solid State Commun.*, 2018, **270**, 92–98.
60 L. J. Wang, A. Kuzmich and A. Dogariu, *Nature*, 2000, **406**, 277–279.
61 M. A. Khan, A. Kashyap, A. K. Solanki, T. Nautiyal and S. Auluck, *Phys. Rev. B*, 1993, **48**, 16974–16978.
62 M. Fox, *Am. J. Phys.*, 2002, **70**, 1269–1270.
63 M. S. Alam, M. Saiduzzaman, A. Biswas, T. Ahmed, A. Sultana and K. M. Hossain, *Sci. Rep.*, 2022, **12**, 8663.
64 D. R. Penn, *Phys. Rev.*, 1962, **128**, 2093–2097.
65 M. Z. Rahaman and A. M. A. Hossain, *RSC Adv.*, 2018, **8**, 33010–33018.
66 W. Tahir, G. M. Mustafa, N. A. Noor, S. M. Alay-e-Abbas, Q. Mahmood and A. Laref, *Ceram. Int.*, 2020, **46**, 26637–26645.
67 M. Asghar, M. W. Iqbal, M. Manzoor, N. A. Noor, M. Zanib, R. Sharma, H. Ullah, S. Aftab and T. Zahid, *Int. J. Energy Res.*, 2022, **46**, 24273–24285.
68 M. Yaseen, H. Shafiq, J. Iqbal, F. Batool, A. Murtaza, M. Iqbal, H. Althib, S. M. Ramay and A. Mahmood, *Phys. B*, 2021, **612**, 412626.
69 M. Manzoor, M. W. Iqbal, M. Imran, N. A. Noor, A. Mahmood, Y. M. Alanazi and S. Aftab, *J. Mater. Res. Technol.*, 2022, **18**, 4775–4785.
70 *Elucidating DFT study on structural, electronic, thermal and elastic properties of SrTcO3 by using GGA and mBJ approach-ScienceDirect*, **https://www.sciencedirect.com/science/article/abs/pii/S0577907317315721**, accessed 20 November 2024.
71 *Phys. Rev. B, 63, 113104, 2001-Large thermoelectric response of metallic perovskites: Sr1−xLaxTiO3 (0 < ∼x < ∼0.1)*, **https://journals.aps.org/prb/abstract/10.1103/PhysRevB.63.113104**, accessed 20 November 2024.
72 S. Hébert, D. Flahaut, C. Martin, S. Lemonnier, J. Noudem, C. Goupil, A. Maignan and J. Hejtmanek, *Prog. Solid State Chem.*, 2007, **35**, 457–467.
73 G. K. H. Madsen and D. J. Singh, *Comput. Phys. Commun.*, 2006, **175**, 67–71.
74 J. Martin, T. Tritt and C. Uher, *J. Appl. Phys.*, 2010, **108**, 121101.
75 V. Chihaia, V. Alexiev, H. S. AlMatrouk, V. Chihaia, V. Alexiev and H. S. AlMatrouk, *Assessment of the Heat Capacity by Thermodynamic Approach Based on Density Functional Theory Calculations*, IntechOpen, 2022.
76 M. Wolf, R. Hinterding and A. Feldhoff, *Entropy*, 2019, **21**, 1058.
77 D. G. Cahill, W. K. Ford, K. E. Goodson, G. D. Mahan, A. Majumdar, H. J. Maris, R. Merlin and S. R. Phillpot, *J. Appl. Phys.*, 2003, **93**, 793–818.
78 *Nanoscale thermal transport. II. 2003–2012: Applied Physics Reviews: Vol 1, No 1*, **https://aip.scitation.org/doi/full/10.1063/1.4832615**, accessed 16 October 2022.
79 J. A. Sharp, W. Meng and W. Liu, *J. Oper. Res. Soc.*, 2007, **58**, 1672–1677.
80 A. Nazir, E. A. Khera, M. Manzoor, A. A. Ghfar, Y. A. Kumar, H. Ullah and R. Sharma, *Solid State Commun.*, 2024, 115622.
81 M. Y. Sofi, M. S. Khan and M. A. Khan, *J. Mater. Chem. C*, 2024, **12**, 16045–16058.
82 A. Ramzan, M. Y. Sofi, M. Ishfaq-ul-Islam, M. S. Khan and M. A. Khan, *RSC Adv.*, 2025, **15**, 24002–24018.
83 A. H. Reshak and S. Auluck, *Comput. Mater. Sci.*, 2015, **96**, 90–95.
84 *Structural and mechanical stabilities, electronic, magnetic and thermophysical properties of double perovskite Ba2LaNbO6: Probed by DFT computation-Mir-2021-International Journal of Energy Research-Wiley Online Library*, **https://onlinelibrary.wiley.com/doi/abs/10.1002/er.6720**, accessed 23 February 2023.
85 A. Nazir, A. Dixit, E. Ahmad Khera, M. Manzoor, R. Sharma and A. J. A. Moayad, *Mater. Adv.*, 2024, **5**, 4262–4275.
86 H. H. Raza, G. Murtaza and R. M. A. Khalil, *Solid State Commun.*, 2019, **299**, 113659.
87 A. Otero-de-la-Roza and V. Luaña, *Phys. Rev. B*, 2011, **84**, 184103.
88 *5.2 Heat Capacity and Specific Heat-Kluitenberg-2002-SSSA Book Series-Wiley Online Library*, **https://acsess.onlinelibrary.wiley.com/doi/abs/10.2136/sssabookser5.4.c49**, accessed 3 October 2024.
89 H. H. Raza, G. Murtaza and M. Shafiq, *Comput. Theor. Chem.*, 2023, **1221**, 114030.
90 A. Wehrl, *Rev. Mod. Phys.*, 1978, **50**, 221–260.